Gravitational Microlensing of the Relativistic Iron Kα Line from Black Hole Accretion Disks

Lisa Fishenfeld

Mentor: Chuck Keeton

Rutgers, the State University of New Jersey

Physics and Astronomy Dept.

136 Frelinghuysen Rd.

Piscataway, NJ 08854

`lisaphy@physics.rutgers.edu`

1.   Introduction

Astrophysicists are eager to learn more about black holes and accretion disks. The existence of black holes (BH) is predicted by general relativity (GR); thus by studying them we learn about gravity and the fabric of space-time. Here we describe a new tool that can help us spatially resolve these elusive objects. Gravitational lensing already magnifies distant bodies through general relativistic effects. Microlensing, in which smaller objects within the lens further lens the image(s), provides a unique insight into the structures of both the source and the lens. When we compound this phenomenon with the study of relativistic iron Kα lines, we open up a new method of exploration. The innermost parts of accretion disks emit X-ray spectra, most prominently the iron Kα line, which are distorted by a combination of Doppler, special relativistic, and general relativistic effects. The shape of the relativistic iron line gives us information about the black hole and accretion disk, including inner and outer radii of iron line emitting region, inclination of disk, and black hole spin. As a black hole undergoes microlensing, different parts of the accretion disk are magnified, and the shape of the relativistic iron Kα line evolves with time. Microlensing effectively gives us higher resolution of the source. By modelling the evolution of the microlensed relativistic emission line, we may gain additional insight into the spatial structure of a black hole and its accretion disk. We discuss gravitational lensing in Sections 2-4, the unified model of active galactic nuclei (AGN) in Section 5, relativistic iron lines in Section 6, microlensing of the iron line in Section 7, and opportunities for further study in Section 8.

2.   Gravitational Lensing Basics

We begin with a review of gravitational lensing, drawing on standard references such as Wambsganss (1998). According to Einstein's theory of general

relativity, mass bends light. Ordinarily, an observer on Earth would see a distant object by the light emitted in Earth's direction. If a body with sufficient mass, such as a galaxy, lies between the source and the observer, it will bend the light such that light rays originally emitted in slightly peripheral directions will be deflected toward the observer by an angle (see Figure 1)

$$\tilde{\alpha} = \frac{4GM(\xi)}{c^2}\frac{1}{\xi} \qquad (1)$$

for a spherical source, where $M(\xi)$ is the lens mass enclosed within an impact parameter ξ. Here we use the *thin lens approximation*, which says that the deflection occurs at the lens plane, since the lens depth is typically much less than the distance between the source and observer. As illustrated in Figure 1, the various angles between the lens, source, and image(s) are described by the lens equation

$$\vec{\beta} = \vec{\theta} - \vec{\alpha}(\vec{\theta}), \qquad (2)$$

where the *reduced deflection angle* between the source and its image is defined as

$$\alpha(\theta) = \frac{D_{LS}}{D_S}\tilde{\alpha}(\theta), \qquad (3)$$

D_{LS} is the distance from the lens to the source, D_S is the distance from the observer to the source, D_L is the distance from the observer to the lens, and $\theta = \xi/D_L$ is the angle between the lens and image (as may be seen in Figure 1). All three distances are angular diameter distances. The lensing has three effects: there may be multiple images, the sum of the images will be brighter than an un-lensed image, and the image(s) themselves will be displaced (and distorted). If the intervening, spherical body, or lens, lies directly in front of the source ($\beta = 0$), the image will appear in the form of a ring with Einstein radius θ_E:

$$\theta_E = \sqrt{\frac{4GM(\theta_E)}{c^2}\frac{D_{LS}}{D_L D_S}}. \qquad (4)$$

An off-center source will produce multiple images. In the approximation where source and lens are both point masses, two images are produced at angles

$$\theta_{1,2} = \frac{1}{2}\left(\beta \pm \sqrt{\beta^2 + 4\theta_E^2}\right). \qquad (5)$$

It was said earlier that the lens body must have sufficient mass. More specifically, the lens must have a sufficiently high two-dimensional surface mass density — the total mass density projected along the line of sight onto a two-dimensional plane (owing to the thin lens approximation):

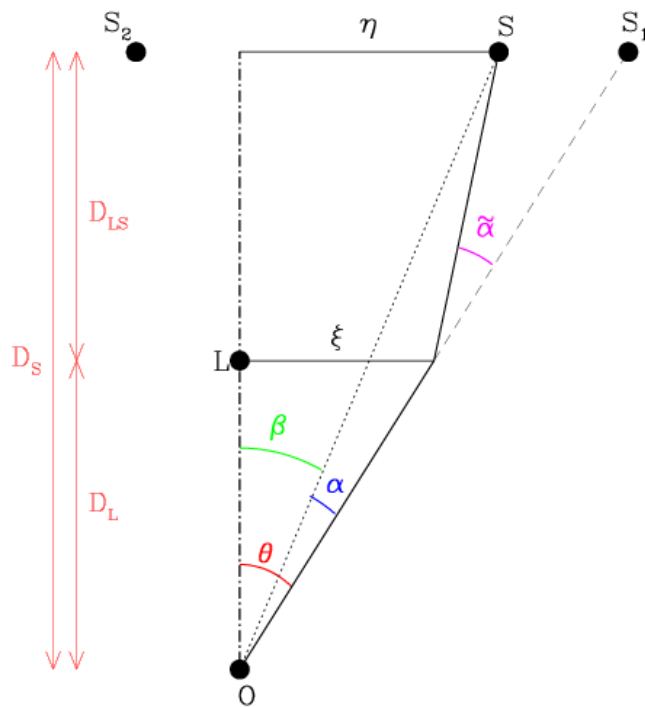$$\Sigma(\vec{\xi}) = \int_0^{D_S} \rho(\vec{r})dz. \qquad (6)$$

Fig. 1.— The relation between the various angles and distances involved in the lensing setup can be derived for the case $\tilde{\alpha} \ll 1$ and formulated in the lens equation (2). [Figure and caption from Wambsganss (1998).]

The critical surface mass density comes from the average density within the Einstein radius (from equation 4):

$$\langle \Sigma \rangle = \frac{M(\theta_E)}{\pi(\theta_E D_L)^2} = \frac{c^2}{4\pi G}\frac{D_S}{D_L D_{LS}} = \Sigma_{crit}. \qquad (7)$$

A lens with $\Sigma > \Sigma_{crit}$ can produce multiple images.

3. Substructure Lensing

Once the overall lens meets the critical surface mass density requirement and gravitational lensing occurs, smaller objects within the lens will further lens the image(s). Referring back to equation (4), the Einstein radius of a lens is proportional to the square root of its mass. Substructure lensing effects are aptly named after the angular size effects they produce: *millilensing* produces lensing effects on the order of milliarcseconds, *microlensing* produces microarcsecond effects, and *nanolensing* exhibits nanoarcsecond effects. A solar mass object such as a star or stellar-mass black hole would have an Einstein radius on the order of microarcseconds (10^{-6} arcseconds). A planet on the order of $10^{-6} M_\odot$ would thus have an Einstein radius on the order of 10^{-9} arcseconds, or nanoarcseconds. Einstein radii of cold dark matter (CDM) substructure depend on the CDM clump's density, as the mass in equation (4) refers to the mass within the Einstein radius. CDM substructure may therefore produce milli-, micro-, or nano- lensing.

These substructure lensing effects may be detected by comparing the flux ratios, relative positions, and time delays of the observed multiple images with their expected values (Treu 2010). For example, in a gravitational lens scenario with four images, the two bright images lying close together are expected to have similar brightness (Pooley et al. 2006). When they do not, such as in quasar PG 1115+080, microlensing is thought to be responsible (Pooley et al. 2006, 2009). If the Einstein radius of the substructure lens is smaller than the source, the substructure lensing effects will not be noticeable; substructure lensing can only affect sources comparable in size or smaller than the Einstein radius (Congdon et al. 2007; Treu 2010).

4. Magnification

As mentioned in Section 2, the lensed image(s) will be magnified, since light originally directed in peripheral trajectories will be bent towards the observer. In general, the magnification is

$$\mu = det\left(\frac{\partial\vec{\theta}}{\partial\vec{\beta}}\right) = det\left(\frac{\partial\vec{\beta}}{\partial\vec{\theta}}\right)^{-1}. \qquad (8)$$

From this equation, it would appear that an Einstein ring ($\beta = 0$) has infinite magnification. Of course, the source is not a point in reality — so while the magnification is very high, it is not infinite in practice.

Magnification depends on the relative angles between the lens, source, and image. In reality, lenses are not points nor homogeneous spheres — they have shapes (approximately circular or elliptical) which contain non-homogeneous surface mass distributions (convergence), and may be subject to internal and external shear (tidal forces from the environment). Such lenses do not produce simple Einstein rings — their magnification profiles depend on their potentials. Locations of formally infinite magnification are called *critical curves* in the plane of the lens (see Figure 2, left panel). When projected onto the source plane, these lines are called *caustics* (see Figure 2, right panel). Smooth caustic lines are *fold caustics*, while the sharp points at which the smooth caustics connect are *cusp caustics*. As shown in the figure, when the source lies outside the outer caustic, one image is produced. Each time the source crosses a fold caustic, the number of images increases or decreases by two. Thus, three or five images are produced when the source is placed in the indicated regions; however, the last (third or fifth) image forms near the center and is highly demagnified and difficult, if not impossible, to observe (Treu 2010).

When adding in substructure lensing effects, the magnification map in the source plane becomes an intricate pattern (see Figure 3). As the source moves through the magnification map it produces a varying number of images and subimages with varying magnifications. Whenever the source crosses a caustic, it is greatly magnified — allowing us to use these caustics as "magnifying glasses".

5. Quasars

A quasar (QSO) is a type of active galactic nucleus (AGN). An AGN is thought to be a supermassive black hole (SMBH) surrounded by an accretion disk with jets emitted perpendicularly to the disk, in turn surrounded by an optically thick gas and dust torus, and finally surrounded by narrow-line clouds (see Figure 4; Carroll & Ostlie 2007).

Estimating the mass and radius of a quasar leads to the theory that a SMBH powers an AGN. The upper limit luminosity of a spherically symmetric object in equilibrium is the Eddington limit: $L_{Ed} \simeq 1.5 \times 10^{31} \frac{M}{M_\odot}$ W (Carroll & Ostlie 2007). A higher luminosity would mean the object is losing mass, or failing to accrete matter. Carroll & Ostlie (2007) cite a typical quasar luminosity to be 5×10^{39} W. Plugging in this luminosity to the Eddington limit equation results in a lower quasar mass limit of $3.3 \times 10^8 M_\odot$. For the radius we turn to a quasar's time variability. If a sphere's surface brightens everywhere at once, there will
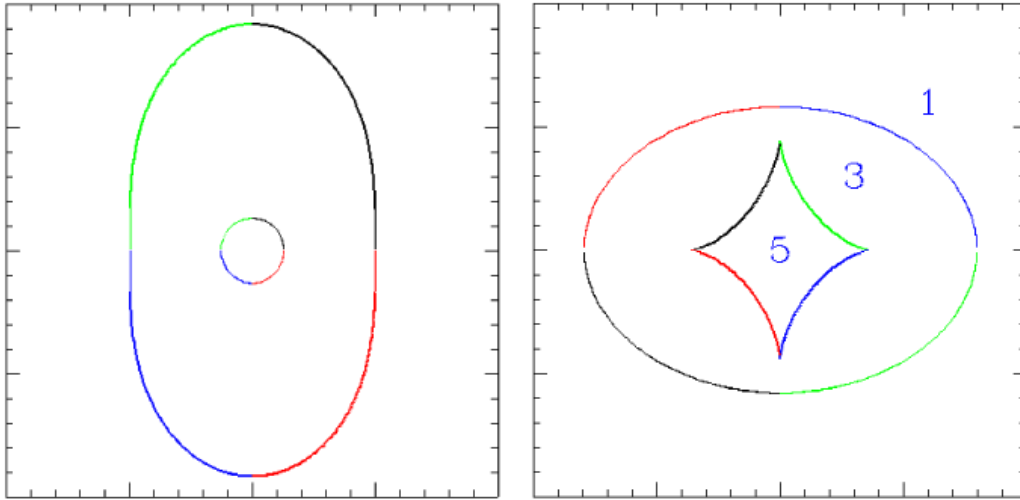
Fig. 2.— The critical curves ([left] panel) and caustics ([right] panel) for an elliptical lens. The numbers in the right panels identify regions in the source plane that correspond to 1, 3 or 5 images, respectively. The smooth lines in the right hand panel are called fold caustics; the tips at which in the inner curve two fold caustics connect are called cusp caustics. [Figure and caption from Wambsganss (1998).]
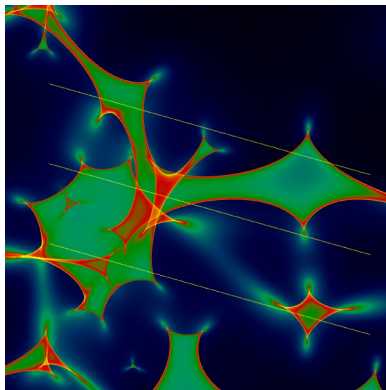

Fig. 3.— Magnification in the source plane, produced by a dense field of stars in the lensing galaxy. The color reflects the magnification as a function of the quasar position: the sequence blue-green-red-yellow indicates increasing magnification. [Figure and caption from Wambsganss (1998).]

be a time delay between receiving light from the closest point of the sphere and the outside edge. If the distance to the closest point is l_1 and the edge is l_2, and the radius of the sphere is R, we get $l_1 + R = l_2 \cos\theta \simeq l_2$ using the small angle approximation. The change in brightness will therefore take about $\Delta t = R/c$. When accounting for the relativistic velocity of a quasar moving away from Earth, we must divide by $\gamma = (1 - v^2/c^2)^{-1/2}$ to get the radius of a quasar as observed on Earth: $R = c\Delta t/\gamma$. With a typical $\Delta t = 1$ hr and a lower limit of $\gamma = 1$, the upper limit on the radius is 1.1×10^{12} m. To fit $M > 3.3 \times 10^8 M_\odot$ into $R < 1.1 \times 10^{12}$ m, we need a supermassive black hole. In fact, the mass of a BH with Schwarzchild radius 1.1×10^{12} m is $3.7 \times 10^8 M_\odot$, which is not much higher than (and on the same order of magnitude as) our lower mass limit.

The large amounts of energy emitted by AGN may be most efficiently produced by accreting matter through a disk around a rotating black hole (Carroll & Ostlie 2007). As matter spirals in toward a BH, the gravitational potential energy it loses gets converted into kinetic energy, which is then converted into heat and light. As a BH spins, it rotates the surrounding spacetime (called *frame dragging*). Any particle in the ergosphere, a region outside a rotating BH where frame dragging is severe, must move along with the BH's rotation. The innermost stable orbit around a rapidly rotating BH lies within its ergosphere, ensuring that the accreting matter will rotate. For these reasons, the unified AGN model includes a rotating accretion disk around a SMBH.

The broad emission lines observed in quasars and Seyfert 1 galaxies (another type of AGN) originate in the broad-line region close to the central BH. The emission line profiles vary on time scales of a month or less, which indicates that the emission region lies near the center, and gives an estimate of their size (Carroll & Ostlie 2007). Quasars take longer to respond to variations, so their broad-line regions may be about four times larger (Carroll & Ostlie 2007). The broad-line region contains optically thick clouds of partially ionized gas, and are kept together by a surrounding high-temperature medium (Carroll & Ostlie 2007).

The various types of observed AGN are believed to be the result of viewing an AGN from different angles. For instance, if one looks at the AGN between the torus and jet, it may appear to be a quasar, Seyfert 1 galaxy, or broad-line radio galaxy (BLRG). However, if one looks through the torus, the AGN may look like a Seyfert 2 galaxy or narrow-line radio galaxy (NLRG).

One argument for unification of the various types of AGN stems from plotting their Hα emission line luminosities vs. their featureless continuum luminosities. If the continuum radiation photoionizes hydrogen that later recombines, producing the Hα emission lines, the two luminosities should be proportional and form a slope 1 line on a log-log plot. This does in fact happen when quasars,

Seyfert 1 and 2 galaxies, BLRGs, and NLRGs are plotted together (the slope is 1.05 ± 0.03; Shuder 1981), suggesting the hydrogen emission lines from these various AGN share a common origin. Another argument involves finding a Seyfert 1 spectrum in the Seyfert 2 galaxy NGC 1068. The two types of Seyferts differ in that Seyfert 1s have both broad and narrow emission lines, while Seyfert 2s exhibit only narrow emission lines. Antonucci & Miller (1985) found broad emission lines in the polarized light of NGC 1068, similar to those found in Seyfert 1 galaxies. If a Seyfert 2 galaxy were viewed through an optically thick torus which obscures the broad lines emitted by the nucleus of a Seyfert 1 galaxy, it would explain the difference between the two objects. In the case of NGC 1068, the Seyfert 1 spectrum reached the observer through light reflected by the interstellar medium (ISM) surrounding the nucleus.

Quasars and Seyfert 1 galaxies both emit broad emission lines; their difference lies in their luminosities. Quasars are brighter, but the luminosity functions of the two do join (Longair 2011). Intermediate-luminosity objects can be classified either as Seyfert 1 galaxies or quasars.

6. Relativistic Iron Lines

An AGN is subject to a number of relativistic effects. The central black hole of a quasar can lens the back of its accretion disk, a type of self-lensing. Armitage & Reynolds (2003) create a relativistic transfer function by integrating photon paths along Schwarzschild geodesics, and use it to map the disk onto the image plane. The effect of this is to flip up the back of the accretion disk, as illustrated in Figure 5. It becomes more pronounced as the inclination angle of the disk increases towards edge-on.

Emission spectra coming from the innermost parts of accretion disks, the strongest of which is iron Kα, are affected by three major shifting effects, producing a distinctive profile. The Doppler effect produces a double-horn shape, where the red-shifted horn results from the side of the accretion disk rotating away from the observer, while the blue-shifted horn is emitted from the side rotating towards us. The special relativistic beaming effect increases the blue-shifted horn. As the light escapes the black hole's gravity, it becomes gravitationally redshifted (a general relativistic effect), which shifts the entire unbalanced double horn in the red direction. The shape of this skewed double horn is determined by the inner radius of the accretion disk, the outer radius of the iron line emitting region, the inclination angle of the accretion disk, and emissivity as a function of radius (Fabian et al. 1989). The innermost stable circular orbit (ISCO), provides information about the black hole's spin (see Figure 6). Although the ISCO may not equal the inner radius which determines the shape of the relativistic iron line,
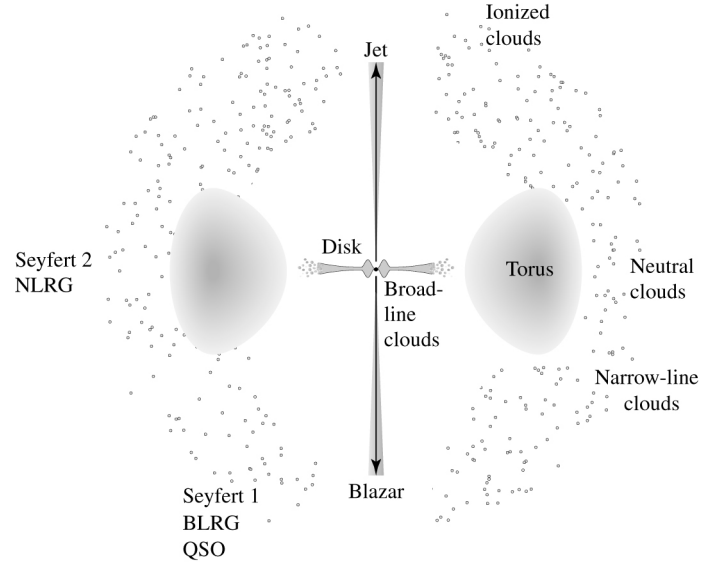
Fig. 4.— Unified model of AGN — AGN type labelled at location of viewing [Figure from Carroll & Ostlie (2007).]
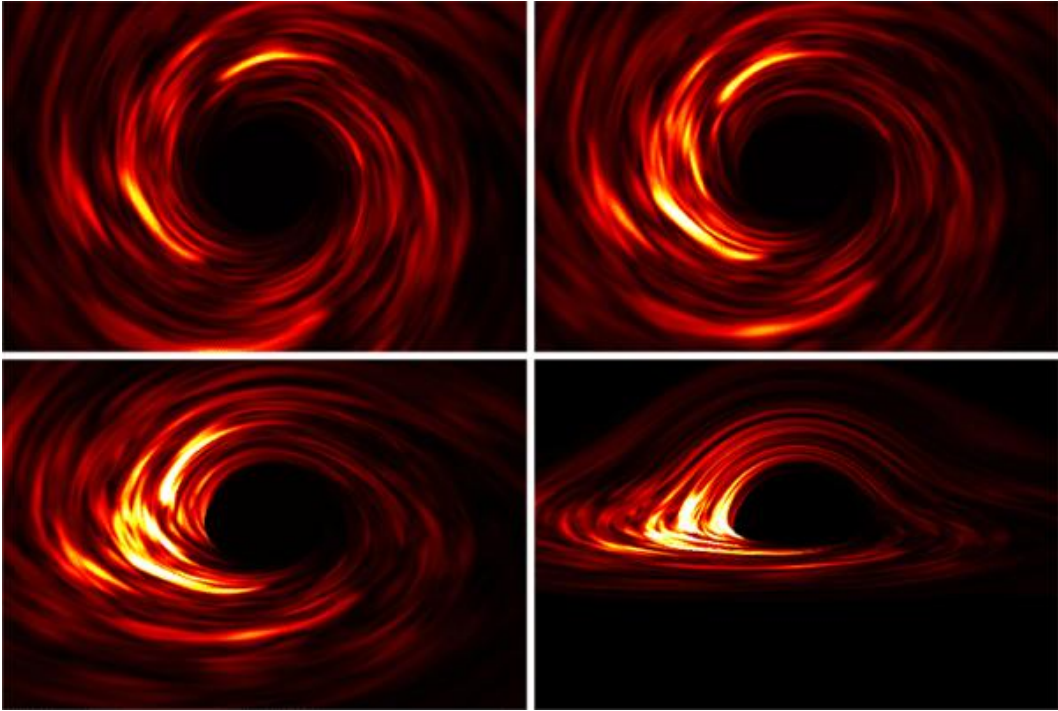

Fig. 5.— View of the disc as seen by a distant observer at an inclination angle of 5° (upper left), 30° (upper right), 55° (lower left) and 80° (lower right). [Figure and caption from Armitage & Reynolds (2003).]

it is believed that the ISCO is no more than one gravitational radius (r_g) outside of it (Fabian & Miniutti 2009). The line profile can also be used to measure the black hole's mass (Stella 1990). By probing into the innermost accretion disk we can detect gravitational light bending and test general relativity.

6.1. Theory

Miller (2007) provides a general review of relativistic X-ray lines from black hole accretion disks. Fabian et al. (1989) model the relativistic iron line of a Schwarzchild black hole by numerically integrating the photon path along the geodesics in the Schwarzchild metric. They visually demonstrate the broadened iron line (Figure 7) as affected by the accretion disk parameters: inner radius r_i, outer radius r_o, inclination i, and emissivity as a function of radius, assumed to follow r^q. The radii are given in terms of the Schwarzchild radius r_s. The top panel shows that the red tail extends as the inner radius decreases, reflecting the greater general relativistic redshift when escaping a deeper gravitational potential. The second panel indicates that as the outer radius increases, the energy separation between the blue and red peaks decreases and the red peak increases in magnitude. In the third panel we see that only the disk inclination affects the upper (blue) edge of the relativistic iron line. In fact, as the inclination increases toward edge-on, the line broadens in both the red and blue directions. A face-on, $i = 0°$ accretion disk has only a single peak (whose line is slightly reddened), as expected with the lack of Doppler shift.

Laor (1991) examines the iron Kα line of a maximal spin Kerr black hole by integrating in the Kerr metric. He plots the iron lines as functions of emission radius and disk inclination. The main differences from the Schwarzchild case were from the emission regions closest to the inner radius. This may be understood by considering that a higher BH spin produces a smaller ISCO, as illustrated in Figure 6. Reynolds & Nowak (2003) demonstrate the iron line as a function of black hole spin for an inclination of $40°$ and an emissivity index of $\beta = 3$ (Figure 8). They give a comprehensive review of relativistic iron lines.

6.2. Observations

Miller (2007) reviews observations of relativistic iron lines in both Seyfert AGN and stellar-mass black holes. He sorts them into three tiers based on strength of evidence for a relativistic iron line, Tier 1 being the strongest. The most widely studied Seyfert AGN relativistic iron line is that of MCG-6-30-15 (Tier 1). Looking at the *Suzaku* spectrum (Reeves et al. 2006) by eye, the iron Kα line looks like a strong, broad emission line peaking at about 6.4 keV
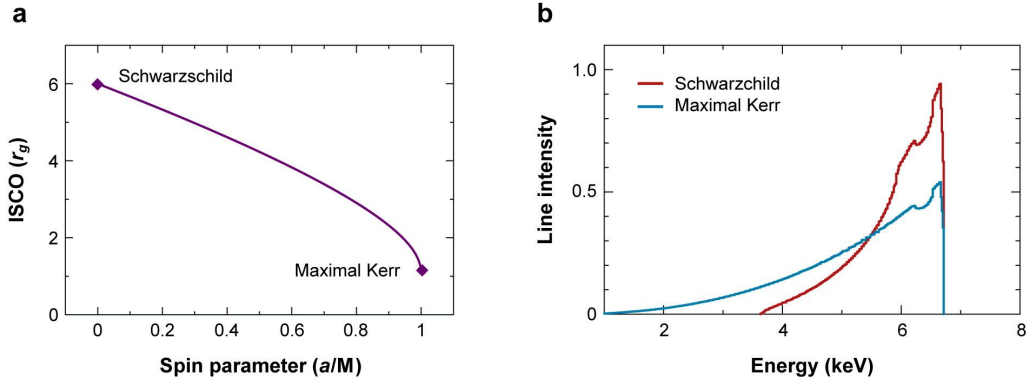
Fig. 6.— $[r_g = GM/c^2, a = c\mathcal{J}/GM^2]$ (a) The dependence of the innermost stable circular orbit (ISCO) on the black hole spin parameter is shown, from Schwarzschild ($a = 0$) to maximal Kerr ($a = 0.998$) solutions. (b) The line profiles predicted in the case of Schwarzschild (red) and maximal Kerr (blue) black holes are shown here. It is the extent of the red wing and its importance relative to the blue wing that allow black hole spin to be determined with disk lines. (Adapted from Fabian & Miniutti 2006.) [Figure and caption from Miller (2007).]
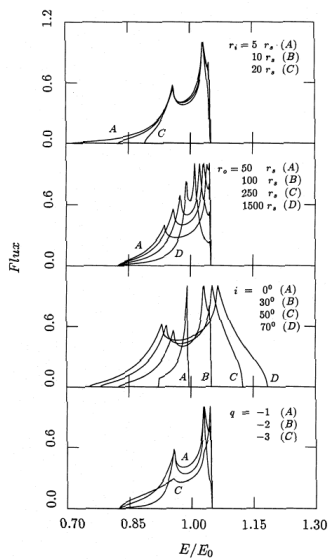
Fig. 7.— Line profiles computed using the method given in the Appendix [of Fabian et al. (1989)]. When not specified, the other parameters are fixed at $r_i = 10r_s$, $r_0 = 100r_s$, $i = 30°$ and $q = -2$. Note that the blue horn is always brighter than the red one and a net redshift only occurs for low inclinations. The small spike on the high-energy side of the blue horn (see curves with $r_i = 10r_s$ and $i = 30°$) is due to radiation emitted by the most blueshifted regions of the disc ($\sim 15r_s$ for $i = 30°$). [Figure and caption from Fabian et al. (1989).]
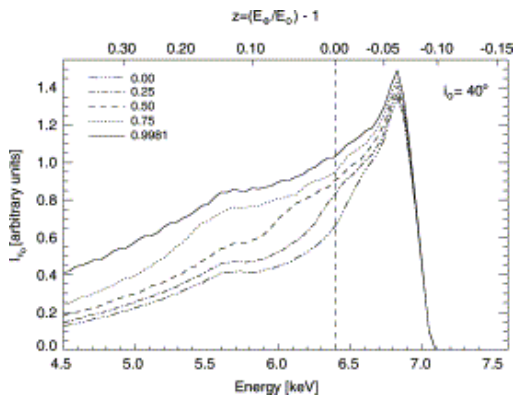

Fig. 8.— Iron line profiles from relativistic accretion disk models as a function of black hole spin parameter. The disk is assumed to extend to the radius of marginal stability with an emissivity index of $\beta = 3$. [Figure and caption from Reynolds & Nowak (2003).]

(the rest energy of the iron Kα line) with a red wing extending to about 3 keV; the double horn shape is present, but not well resolved. Using *XMM-Newton* data, Brenneman & Reynolds (2006) find a spin of $a = 0.989^{+0.009}_{-0.002}$ (at 90% confidence), inclination $i = 29.699 \pm 0.709°$, $r_{min} = 1.615 \pm 0.074 r_g$, and $r_{max} = 397.028 \pm 494.559 r_g$, where $r_g = GM/c^2$. Other Tier 1 Seyfert AGN whose relativistic iron lines have been observed include 3C 120 (Reeves et al. 2006), NGC 2992 (Yaqoob et al. 2007; Reeves et al. 2006), MCG-5-23-16 (Reeves et al. 2006, 2007), NGC 3516 (Turner et al. 2002; Markowitz et al. 2006), NGC 3783 (Nandra et al. 2006), NGC 4051 (Nandra et al. 2006; Ponti et al. 2006; Reeves et al. 2006), NGC 4151 (Nandra et al. 2006), and Mrk 766 (Mason et al. 2003; Nandra et al. 2006). Relativistic iron lines have been detected in AGN as far as redshift $z \simeq 2$ (Miller 2007).

The study of relativistic iron lines was historically motivated by observation of Cygnus X-1, a stellar mass black hole. Studies of this BH show inconclusive, even contradictory, models. For example, Duro et al. (2011) demonstrate that the *XMM-Newton* observation of the iron Kα line may be explained either by a low-spin black hole whose emissivity is highly concentrated near the inner radius of the disk, or by a high-spin black hole with expected emissivity $\propto r^{-3}$. In the latter case, the spin is determined by fixing the emissivity profile in the model, whereas the emissivity is allowed to vary in the former. Since the ISCO decreases as BH spin increases, emission extremely close to the larger ISCO of the low-spin BH may correspond to a similar radius as emission spread out over a region that extends to the smaller ISCO of a high-spin BH. Other relevant Tier 1 stellar-mass black holes include XTE J1550-564, XTE J1650-500, GRO J1655-40, GX 339-4, SAX J1711.6-3808, and GRS 1915+105 (see Miller 2007, for references).

7. Microlensing of Iron Kα Line

Since the relativistic iron lines are emitted from the innermost area of an accretion disk, this line emitting region may be treated as a smaller source than the optical emitting region. Recall from Section 3 that substructure lensing affects sources smaller than or comparable in size to the Einstein radius. The iron line emitting region may therefore be subject to microlensing or possibly nanolensing, even if the entire quasar is too large. X-ray observations support this; X-ray flux ratio anomalies are found to be about six times stronger than in the optical (Pooley et al. 2006), indicating that the X-ray emitting region is more strongly affected by microlensing than the optical region. As a source passes across a caustic, the part of the source lying on the caustic line is highly magnified, so the emission spectrum is dominated by light originating in that

part. The relativistic shifting effects selectively influence various parts of the iron line emission region; therefore, while the source is passing a caustic, the iron line profile changes with time. This effectively gives us higher resolution of the accretion disk area closest to the black hole.

7.1. Theory

Popović et al. (2003) model the evolution of a microlensed iron Kα line using a ray tracing method to account for self-lensing. The two cases examined are microlensing by an isolated compact object, and microlensing by a straight fold caustic. For each case they model both the Schwarzchild (non-spinning BH) and Kerr (spinning BH) metrics. They do not discuss how to recover the quasar parameters (inner and outer radii of iron line emitting region, BH spin, etc.) from the evolution of the iron Kα line. Furthermore, these microlensing models are limited. The first case is artificial and neglects the complexity of microlensing within the framework of a macrolens. A compact object whose Einstein radius is appropriately small to create microlensing would not be sufficient to gravitationally lens a quasar if it were isolated — it must be part of a larger lens. The caustic of an isolated point mass lens is a single point, whereas a point mass microlens within a lensing galaxy would produce a magnification map such as Figure 3 (which in fact reflects a collection of stars within a galaxy macrolens).

The second scenario, that of a straight fold caustic, is more robust. If the accretion disk is sufficiently small, a fold caustic could be straight in a local approximation. As an example, the straight, yellow lines in Figure 3 indicate the paths a quasar might take as it passes through the magnification map in the source plane. If one were to zoom in on a point where the yellow path crosses a fold caustic, the caustic may be approximated as a straight line compared to the size of the quasar's iron line emitting region. This approximation would break down if the accretion disk were larger in comparison to the curvature of the fold caustic.

Popović et al. (2006) expand upon their previous work by modelling three orientations of the BH rotation axis with respect to the approaching, straight-line caustic, as well as microlensing by a more realistic caustic magnification pattern. They maintain a common BH mass, disk inclination, and lens mass, however. They show the resulting light curves and spectrum changes, and find that their models are consistent with observations (discussed below) if the iron Kα line originates from the innermost region of the accretion disk while the X-ray continuum emitting region is larger.

Jovanovic (2005) wrote a PhD thesis on this topic; unfortunately, it was only published in the Serbian language. An English summary may be found

in Jovanović (2006). He modelled the microlensing of an accretion disk using a point microlens, straight-fold caustic, and quadruple microlens (microlensing pattern). The conclusions summary reflects the findings of Popović et al. (2003, 2006); a more detailed analysis may be described in the thesis itself.

7.2. Observations

Microlensing of quasar iron line emission has been observed in at least nine quasars: MG J0414+0534 (Chartas et al. 2002), H1413+117 (Chartas et al. 2004), QSO 2237+0305 (Dai et al. 2003; Chen et al. 2012), QJ 0158-4325 (Chen et al. 2012), HE 0435-1223 (Chen et al. 2012), HE 1104-1805 (Chen et al. 2012), SDSS 0924+0219 (Chen et al. 2012), SDSS 1004+4112 (Chen et al. 2012), and RX J1131-1231 (Chartas et al. 2012).

The earlier studies do not follow the time evolution of the iron Kα line as it is microlensed (Chartas et al. 2002; Dai et al. 2003; Chartas et al. 2004). They determine microlensing of the iron line by comparing the multiple images, and finding the strength or equivalent width of the iron line to be higher in only one image. In order for only one image to be affected, the variation cannot originate at the source; the other option would be a variation at the lens plane. An increased magnification in one image suggests substructure lensing. Through modelling, Popović et al. (2006) confirm that the iron line enhancements are consistent with microlensing. One recent study does take spectra across multiple epochs in six gravitationally lensed quasars (Chen et al. 2012), which could theoretically track the time evolution of the iron line. Due to the low signal to noise ratios of the individual epochs, however, they have to combine the spectra, which obscures the temporal microlensing effects. The latest study successfully follows the evolution of a microlensed iron Kα line across three periods (Figure 9; Chartas et al. 2012). Although they do not model the iron line time evolution, they estimate a "radius of line emitting region" of $15r_g$ and a disk inclination of 10^{+2}_{-2} degrees based on the iron line profile during the second period.

8. Further Study

To make use of this tool, further work must be done both in theory and observation. Models of the microlensing transformations of the relativistic iron line for various black hole/accretion disk parameters can be compared to find possible signatures which would allow us to extract these parameters from monitoring observations. The effects of nanolensing — substructure lensing caused by an object on the order of a planet or subsolar mass dark matter halo — on iron line evolution have yet to be explored. Nanolensing occurs on a smaller
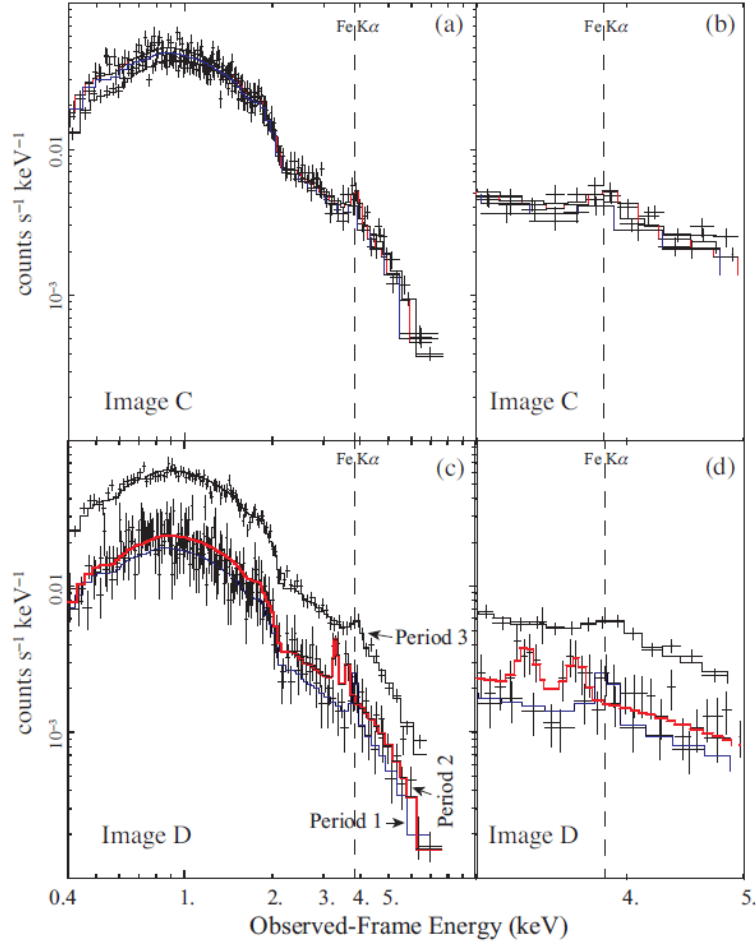
Fig. 9.— Stacked spectra of images C [not microlensed] (panel a) and D [microlensed] (panel c) for three periods. A close-up of the stacked spectra around the Fe Kα region for images C (panel b) and D (panel d). The curves are the best-fit absorbed power-law plus Gaussian line models. [Figure and caption from Chartas et al. (2012).]

scale than microlensing, which would further probe the spatial dimensions of the source since it would only affect sources on the order of a nanoarcsecond or smaller. A straight fold caustic would no longer be applicable, and the intricacies of nanolensing caustics may produce different effects. Thus far we have concentrated on using this method to analyze the source (BH and accretion disk). It would be interesting to see if the micro- or nano- lens properties could be analyzed this way. If we could differentiate between a star, CDM halo, or free-floating planet by the way it lenses the iron Kα line, this tool would become doubly useful. A rich theoretical analysis that highlights what may be learned from microlensing of the iron line, and how, would motivate and guide new, detailed observational campaigns. Such efforts may include more time-evolution observations, such as done by Chartas et al. (2012), and modelling of the results, not merely for a single epoch, but for the development of the iron line. The potential avenues of study are plentiful, making the microlensing (or nanolensing) of the relativistic iron Kα line a tool worthy of development.

REFERENCES

Antonucci, R. R. J., & Miller, J. S. 1985, ApJ, 297, 621

Armitage, P. J., & Reynolds, C. S. 2003, MNRAS, 341, 1041, arXiv:astro-ph/0302271

Brenneman, L. W., & Reynolds, C. S. 2006, ApJ, 652, 1028, arXiv:astro-ph/0608502

Carroll, B., & Ostlie, D. 2007, An introduction to modern astrophysics, 2nd edn. (Pearson Addison-Wesley)

Chartas, G., Agol, E., Eracleous, M., Garmire, G., Bautz, M. W., & Morgan, N. D. 2002, ApJ, 568, 509, arXiv:astro-ph/0112112

Chartas, G., Eracleous, M., Agol, E., & Gallagher, S. C. 2004, ApJ, 606, 78, arXiv:astro-ph/0401240

Chartas, G., Kochanek, C. S., Dai, X., Moore, D., Mosquera, A. M., & Blackburne, J. A. 2012, ArXiv e-prints, 1204.4480

Chen, B., Dai, X., Kochanek, C. S., Chartas, G., Blackburne, J. A., & Morgan, C. W. 2012, ArXiv e-prints, 1202.5304

Congdon, A. B., Keeton, C. R., & Osmer, S. J. 2007, MNRAS, 376, 263, arXiv:astro-ph/0612542

Dai, X., Chartas, G., Agol, E., Bautz, M. W., & Garmire, G. P. 2003, ApJ, 589, 100, arXiv:astro-ph/0301592

Duro, R. et al. 2011, A&A, 533, L3, 1108.1157

Fabian, A. C., & Miniutti, G. 2009, in The Kerr spacetime : rotating black holes in general relativity, ed. D. L. Wiltshire, M. Visser, & S. Scott (Cambridge University Press, Cambridge, England)

Fabian, A. C., Rees, M. J., Stella, L., & White, N. E. 1989, MNRAS, 238, 729

Jovanovic, P. 2005, PhD thesis, PhD Thesis, Faculty of Mathematics, University of Belgrade

Jovanović, P. 2006, PASP, 118, 656, arXiv:astro-ph/0602035

Laor, A. 1991, ApJ, 376, 90

Longair, M. 2011, High Energy Astrophysics (Cambridge University Press)

Markowitz, A. et al. 2006, Astronomische Nachrichten, 327, 1087

Mason, K. O. et al. 2003, ApJ, 582, 95, arXiv:astro-ph/0209145

Miller, J. M. 2007, ARA&A, 45, 441, 0705.0540

Nandra, K., O'Neill, P. M., George, I. M., Reeves, J. N., & Turner, T. J. 2006, Astronomische Nachrichten, 327, 1039, arXiv:astro-ph/0610585

Ponti, G., Miniutti, G., Cappi, M., Maraschi, L., Fabian, A. C., & Iwasawa, K. 2006, MNRAS, 368, 903, arXiv:astro-ph/0602191

Pooley, D., Blackburne, J. A., Rappaport, S., Schechter, P. L., & Fong, W.-f. 2006, ApJ, 648, 67, arXiv:astro-ph/0604152

Pooley, D., Rappaport, S., Blackburne, J., Schechter, P. L., Schwab, J., & Wambsganss, J. 2009, ApJ, 697, 1892, 0808.3299

Popović, L. Č., Jovanović, P., Mediavilla, E., Zakharov, A. F., Abajas, C., Muñoz, J. A., & Chartas, G. 2006, ApJ, 637, 620

Popović, L. Č., Mediavilla, E. G., Jovanović, P., & Muñoz, J. A. 2003, A&A, 398, 975, arXiv:astro-ph/0211523

Reeves, J. N. et al. 2007, PASJ, 59, 301, arXiv:astro-ph/0610434

——. 2006, Astronomische Nachrichten, 327, 1079, arXiv:astro-ph/0610436

Reynolds, C. S., & Nowak, M. A. 2003, Phys. Rep., 377, 389, arXiv:astro-ph/0212065

Shuder, J. M. 1981, ApJ, 244, 12

Stella, L. 1990, Nature, 344, 747

Treu, T. 2010, ARA&A, 48, 87, 1003.5567

Turner, T. J. et al. 2002, ApJ, 574, L123, arXiv:astro-ph/0206223

Wambsganss, J. 1998, Living Reviews in Relativity, 1, 12, arXiv:astro-ph/9812021

Yaqoob, T. et al. 2007, PASJ, 59, 283